High-Resolution 2-D Sector-Scan Imaging Using MIMO Sonar with Narrowband LFM Pulses

Chao SUN *, *Member*, *IEEE*, Xiong-hou LIU, *Student Member*, *IEEE*, Jie ZHUO, *Member*, *IEEE,* Zong-wei LIU
Institute of Acoustic Engineering, Northwestern Polytechnical University, Xi'an 710072, China

Emails: csun@nwpu.edu.cn; eliuxionghou@gmail.com; jzhuo@nwpu.edu.cn; eliuzongwei@gmail.com

***Abstract*—For obtaining high cross-range resolution, a new sector-scan imaging approach based on a multiple-input multiple-output (MIMO) sonar is proposed in this paper. The MIMO sonar is composed of two transmitting sensors and a receiving uniform linear array (ULA), which are located on the same straight line. The spacing between two transmitting sensors is equal to the product of the sensor number and the sensor spacing of the receiving ULA. Furthermore, two narrowband linear frequency modulation (LFM) pulses, sharing the same frequency band but opposite modulation slopes, are employed as transmitting waveforms. In addition, the phase-shifting beam-forming is conducted on the outputs of matched filters. Via theoretical analysis and numerical simulation, it is shown that the MIMO sonar doubles the cross-range resolution, when compared to the traditional 2-D sector-scan sonar.**

***Index Terms*—underwater acoustics; sonar imaging; 2-D imaging; sector-scan imaging; multiple-input multiple-output (MIMO) sonar; sector-scan sonar; high resolution**

I. INTRODUCTION

Sector-scan imaging sonar usually uses a transducer to transmit a wide beam and illuminate an underwater area during a single ping. At the receiving end, a linear array is used to receive and beamform echoes scattered back from the probing area. Picking up intensities of each beam according to echoes' arriving time, the 2-D sector-scan image is generated [1]. Such sector-scan sonar system can be handled by a frog-man, or equipped onto underwater platforms, such as towed bodies, autonomous underwater vehicles (AUVs), or remotely operated vehicles (ROVs) to carry out the searching, object identification, and mapping assignment [2-4].

For obtaining high-resolution 2-D sector-scan images, the range and cross-range resolutions play two important roles. The range resolution is basically determined by the bandwidth of the transmitting waveform, and the cross-range resolution is directly determined by the effective aperture of the imaging array [1, 5]. To increase the range resolution, using the waveform with a wide bandwidth will be useful. However, the cross-range resolution of the sector-scan sonar decreases with the increase of the probing range. Thus, for obtaining a fine cross-range resolution, lengthening the array physical size or adopting waveforms of higher frequencies is inevitable [1]. Nevertheless, lengthening the array size will leads to the imaging array too big to be carried by underwater platforms. Similarly, using waveforms of higher frequencies requires more sensors to suppress possible grating lobes caused by spatial under-sampling, as well as shorter probing range due to higher absorption loss. Therefore, a sector-scan imaging approach, which can obtain better cross-range resolution without using larger-size array or higher-frequency waveforms, is in demand.

Considering shortcomings of traditional sector-scan imaging systems, a new imaging approach based on a narrowband multiple-input multiple-output (MIMO) sonar is proposed in this paper. Specifically, the MIMO sonar is composed of two transmitting sensors and a receiving uniform linear array (ULA). The two transmitting sensors and the receiving ULA are located on the same straight line and centered at the origin of Cartesian coordinate. And the sensor spacing of two transmitting sensors is equal to the product of the sensor spacing and the sensor number of the receiving ULA. Furthermore, different from complicated coded waveforms used in other MIMO arrays [6-12], two narrow-band LFM pulses are adopted as transmitting waveforms of the proposed MIMO sonar. For meeting the requirement on auto- and cross-correlation functions of transmitting wave-forms mentioned in Ref. [11], the two LFM pulses are designed to share the same frequency band but opposite modulation slopes. Due to the same frequency band, the two LFM pulses share the same auto-correlation function (i.e., the sinc function). And meanwhile, the cross-correlation function is low enough to be ignored due to opposite modulation slopes. In addition, to get enhanced echoes of different beams, the phase-shifting beamforming is conducted on the outputs of matched filters. Successfully, the proposed MIMO sonar obtains twice cross-range resolution than a typical sector-scan imaging system using a single-input multiple-output (SIMO) sonar.

The remainder of this paper is organized as follows. In Section II, the configuration of MIMO sonar is proposed. The high-resolution sector-scan imaging procedure using the MIMO sonar is introduced in Section III. In Section IV, numerical examples are presented for testing our imaging approach. Finally, our conclusions are given in Section IV.

978-0-933957-40-4 ©2013 MTS

II. ARRAY CONFIGURATION OF MIMO SONAR

The MIMO sonar is composed of two transmitting sensors and an N-sensor receiving ULA, which are located on the same straight line and centered at the origin of Cartesian coordinate. Let d_t denote the inter-sensor spacing between two transmitting sensors and d_r denote that of the receiving ULA, which satisfy

$$d_t = Nd_r \tag{1}$$

In this case, the MIMO sonar is equivalent to a virtual SIMO sonar. The virtual SIMO sonar is composed of a single transmitting sensor located at the center of Cartesian coordinate and a receiving ULA with $2N$ sensors and d_r as the spacing.

For comparison, suppose that there is a real SIMO sonar composed of a single transmitting sensor and (N+1)-sensor receiving ULA with d_r as the inter-sensor spacing. Apparently, the SIMO sonar shares the same sensor number (i.e., N+2) and array physical size (i.e., Nd_r) as the MIMO sonar. However, the effective aperture of the MIMO sonar is two-time bigger than that of the SIMO sonar, which is explained as follows.

According to the array configuration and sensor number, the physical size of the MIMO sonar, L_{MIMO}, is equal to

$$L_{\mathrm{MIMO}} = Nd_r \tag{2}$$

And the effective aperture of the MIMO sonar, D_{MIMO}, is equal to the aperture of the virtual SIMO sonar, i.e.,

$$D_{\mathrm{MIMO}} = \left(2N-1\right) d_r \tag{3}$$

The physical size of the SIMO sonar, L_{SIMO}, and the corresponding effective aperture, D_{SIMO}, are the same, which can be expressed as

$$L_{\mathrm{SIMO}} = D_{\mathrm{SIMO}} = Nd_r \tag{4}$$

From Eqs. (2)- (4) we can see that the physical size of the MIMO and SIMO sonars are the same, i.e.,

$$L_{\mathrm{MIMO}} = L_{\mathrm{SIMO}} \tag{5}$$

And the relationship between effective apertures of the two sonars is

$$D_{\mathrm{MIMO}} = \frac{2N-1}{N} D_{\mathrm{SIMO}} \tag{6}$$

In terms of a sector-scan sonar, the sensor number of receiving array, N, is often set to be big enough to get a fine cross-range resolution. Thus, when the receiving sensor number, N, is a large value (dozens of or hundreds of), Eq. (6) can be directly simplified as

$$D_{\mathrm{MIMO}} = 2D_{\mathrm{SIMO}} \tag{7}$$

From the above discussion, it is known that the MIMO sonar doubles the cross-range resolution, when compared to a SIMO sonar with the same physical size and sensor number. The better cross-range resolution is obtained without lengthening the array physical size or adopting waveforms of higher frequencies. For illustrating more clearly, the MIMO sonar with two transmitting and twenty-four receiving sensors, the equivalent virtual SIMO sonar, and a real SIMO sonar sharing the same physical size and sensor number as the MIMO sonar, are depicted in Fig. 1. In Fig. 1, the solid circle stands for the real transmitting sensor, the hollow one stands for the real receiving sensor, and the shadow one stands for the virtual receiving sensor. Furthermore, in Fig. 1(c), a receiving sensor is superposed with the single transmitting sensor at the coordinate origin.

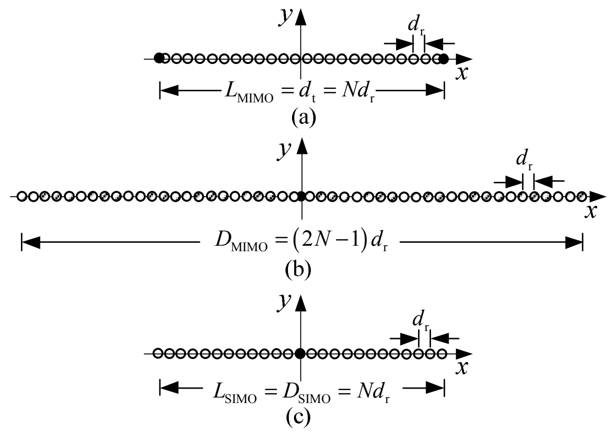

Fig. 1 Array configurations of (a) MIMO sonar with two transmitting and twenty-four receiving sensors, (b) virtual SIMO sonar with one transmitting and forty-eight receiving sensors, and (c) real SIMO sonar with one transmitting and twenty-five receiving sensors.

III. SECTOR-SCAN IMAGING PROCEDURE

Assume that the two transmitting sensors of the MIMO sonar emit two narrowband LFM pulses simultaneously. The two transmitting LFM pulses share the same pulse duration T and frequency band B, but with opposite modulation directions. In other words, the frequency band of one LFM pulse is from f_1 up to f_2, and that of the other one is from f_2 down to f_1, where f_2-f_1=B. The two LFM pulses can be expressed as

$$s_1(t) = 1/\sqrt{T}\mathrm{rect}\left(t/T\right)\exp\left[\mathrm{j}2\pi\left(f_1 t + 0.5Bt^2/T\right)\right] \tag{8}$$

$$s_2(t) = 1/\sqrt{T}\mathrm{rect}\left(t/T\right)\exp\left[\mathrm{j}2\pi\left(f_2 t - 0.5Bt^2/T\right)\right] \tag{9}$$

Considering such a scenario that the MIMO sonar carrier is still or its moving speed is much smaller than the sound propagation speed in water, the time delay due to the relative motion can be ignored during a single snapshot illumination. And accordingly, the Doppler shift is also ignored due to the low relative speeds of MIMO sonar and target. Furthermore, we assume that the MIMO sonar is working in the mono-static mode and far-field condition. For simplification, the far-field target to be imaged is modeled as P ideal scatterers and the pth (p=1, 2,⋯,P) scatterers locates in the angle of θ_p. The echo re-

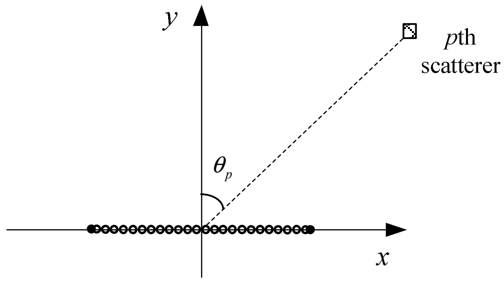

Fig. 2 2-D coordinate system of MIMO sonar (two transmitting and twenty-four receiving sensors) and the *p*th scatterer

flected back from the *p*th scatterer and received by the *N* receiving sensors is supposed to be fully correlated across the receiving ULA. As an example, the 2-D coordinate system of the MIMO sonar (composed of two transmitting sensors and twenty-four receiving sensors, as shown in Fig .1(a)) and the location of the *p*th scatterer is depicted in Fig. 2.

For simplifying the analysis further, the transmission loss associated with the free-space propagation to the reference point of the MIMO sonar (i.e., the origin of Cartesian coordinate) is ignored and so is the medium absorption. According to the above assumption, the echo at the *n*th (n=1, 2, ⋯, N) receiving sensor can be simplified as the summation of two LFM pulses with different time delays. Let $x_n(t)$ denote echoes at the *n*th receiving sensor, then we have [11]

$$x_n(t)=\sum_{p=1}^{P}\sigma_p\sum_{m=1}^{2}s_m(t-\tau_{tm}^p-\tau_{rn}^p)+z_n(t) \tag{10}$$

where σ_p denotes the reflectivity of the *p*th scatterer, τ_{tm}^p denotes the sound propagation time delay from the *m*th (m=1, 2) transmitting sensor to the *p*th scatterer, τ_{rn}^p denotes the time delay from the *p*th scatterer to the *n*th (n=1, 2, ⋯, N) receiving sensor, and $z_n(t)$ denotes the white Gaussian noise at the *n*th receiving sensor, which is independent with the two transmitting LFM pulses.

Let $h_m(t)$ denote the impulse response function of the matched filter corresponding to the *m*th (m=1, 2) transmitting waveform, we get

$$h_m(t)=\left[s_m(T-t)\right]^{c} \tag{11}$$

where $[\ ]^{c}$ denotes the complex conjugate.

Filtering echoes at *N* receiving sensors with two matched filters, 2*N* outputs are obtained. The [(m-1)N+n]th output is obtained by filtering the echo at the *n*th receiving sensor using the *m*th matched filter, which is given by

$$\begin{aligned}y_{(m-1)N+n}(t)&=x_n(t)*h_m(t)\\&=\sum_{p=1}^{P}\sigma_p\sum_{m=1}^{2}s_m(t-\tau_{tm}^p-\tau_{rn}^p)*h_m(t)+\\&\quad z_n(t)*h_m(t)\end{aligned} \tag{12}$$

where $*$ denotes the convolution.

Since the Doppler shift can be ignored, the matched filter can be considered a correlator. In other words, when the two transmitting LFM pulses are independent with noise at all receiving sensors (i.e., $z_n(t)*h_m(t)=0$), the outputs of the matched filter can be simplified as the summation of auto- and cross- correlation functions:

$$\begin{aligned}y_{(m-1)N+n}(t)=\sum_{p=1}^{P}\sigma_p\Big[&R_m\left(t-\tau_{tm}^p-\tau_{rn}^p-T\right)+\\&R_{1,2}\left(t-\tau_{ti}^p-\tau_{rn}^p-T\right)\Big]\end{aligned} \tag{13}$$

where $R_m(t)$ (m=1, 2) denotes the auto-correlation function of the *m*th (m=1, 2) transmitting waveform, and $R_{1,2}(t)$ denotes the cross-correlation function between two transmitting LFM pulses.

Under the condition that the modulation slopes of the two LFM pulses are opposite with each other, the cross-correlation function is low enough (compared to the peak value of the auto-correlation function) to be ignored. And hence, Eq. 13 can be simplified as [11]:

$$y_{(m-1)N+n}(t)=\sum_{p=1}^{P}\sigma_pR_m(t-\tau_{tm}^p-\tau_{rn}^p-T) \tag{14}$$

Further, since the frequency bands of the two LFM pulses are superposed with each other, the corresponding two auto-correlation functions are the same:

$$\begin{aligned}R_1(t)=R_2(t)&=\left(T-|t|\right)\mathrm{sinc}\left[\pi\frac{B}{T}\left(T-|t|\right)\right]\times\\&\exp\left[\mathrm{j}2\pi\left(\frac{f_1+f_2}{2}\right)t\right]\\&=\widetilde{R}_1(t)\exp\left[\mathrm{j}2\pi\left(\frac{f_1+f_2}{2}\right)t\right]\end{aligned} \tag{15}$$

where $\widetilde{R}_1(t)$ denotes the baseband envelope of $R_1(t)$.

Consequently, outputs of matched filters can be simplified as the summation of the auto-correlation function $R_1(t)$ with different time delays:

$$\begin{aligned}y_{(m-1)N+n}(t)&=\sum_{p=1}^{P}\sigma_pR_1(t-\tau_{tm}^p-\tau_{rn}^p-T)\\&=\sum_{p=1}^{P}\sigma_p\widetilde{R}_1(t-\tau_{tm}^p-\tau_{rn}^p-T)\times\\&\quad\exp\left[\mathrm{j}2\pi\left(\frac{f_1+f_2}{2}\right)\left(t-\tau_{tm}^p-\tau_{rn}^p-T\right)\right]\end{aligned} \tag{16}$$

According to Eq. 16, the time delay of the peak of the [(m-1)N+n]th pulse-compressed echo (i.e., the time delay of the [(m-1)N+n]th matched filter) reflected back from the *p*th scatterer is equal to the time delay $\tau_{t,m}^p+\tau_{r,n}^p$ plus the constant time delay of the matched filter *T*, as

$$\begin{aligned}\tau_{(m-1)N+n}^p&=\tau_{t,m}^p+\tau_{r,n}^p+T\\&=2\tau_0^p+T+(\tau_{t,m}^p-\tau_0^p)+(\tau_{r,n}^p-\tau_0^p)\end{aligned} \tag{17}$$

For the MIMO sonar working in the far field situation, ignoring common constant time delay $2\tau_0^p + T$, Eq. 17 can be rewritten as

$$\begin{aligned}\tau_{(m-1)N+n}^p &= (\tau_{t,m}^p - \tau_0^p) + (\tau_{r,n}^p - \tau_0^p) \\ &= \left[(m-1)N + n - 1 - \frac{2N-1}{2}\right]\frac{d_r \sin(\theta_p)}{c}\end{aligned} \tag{18}$$

Based on Eqs. 16 and 18, we can see that the outputs of all matched filters are narrowband signals, with $\widetilde{R}_1(t)$ as the baseband envelope and $(f_1+f_2)/2$ as the center frequency. The time delay between two neighboring outputs of matched filters is equal to $d_r\sin(\theta_p)/c$. Thus, Eq. 16 can be considered the pulse-compressed echoes of a virtual SIMO sonar with $2N$ receiving sensors and d_r as the spacing. As a result, the narrowband beamforming methods for an ULA can be applied to the $2N$ outputs of matched filters. Without loss of generality, the phase-shifting beamforming can be expressed as

$$B_q(t) = \sum_{m=1}^{2}\sum_{n=1}^{N}\left[w_{(m-1)N+n}\right]^c y_{(m-1)N+n}(t) \tag{19}$$

where $B_q(t)$ denotes the output of the qth beam,

$$w_{(m-1)N+n} = A_{(m-1)N+n}^q \exp\left[-j2\pi\left(\frac{f_1+f_2}{2}\right)\tau_{(m-1)N+n}^q\right] \tag{20}$$

denotes the complex weighting, $A_{(m-1)N+n}^q$ denotes the amplitude weighting, and $\tau_{(m-1)N+n}^q$ is calculated from Eq. 18 by re- placing the angle of the scatterer θ_p as the beam steering direction θ_q. Getting enhanced echoes by forming beams in different directions and picking up intensities, the 2-D sector- scan image is obtained at last.

IV. Computer Simulation

The MIMO sonar with two transmitting and twenty-four receiving sensors is adopted in the simulation, as depicted in Fig. 1(a). For performance comparison, a SIMO sonar with one transmitting and twenty-five receiving sensors is used, as shown in Fig. 1(c). Both MIMO and SIMO sonars are located on the x axis and centered at the coordinate origin. The inter-sensor spacing of the MIMO sonar satisfy that $d_t=24d_r=24\lambda/2$, and that of the receiving ULA in the SIMO sonar is $d_r=\lambda/2$, where λ denotes the wavelength corresponding to the center frequency of the transmitting pulse. According to previous discussion in Section II, the MIMO and SIMO sonars share the same sensor number and physical size (i.e., 12λ).

As mentioned above, the two transmitting sensors of the MIMO sonar emit two LFM pulses simultaneously. The center frequency of two LFM pulses is $(f_1+f_2)/2=400$ kHz with a $B=20$ kHz bandwidth, and the pulse duration T is 8 ms. In other words, the frequency bands of the two LFM pulses are 390 kHz-410 kHz and 410 kHz-390 kHz, respectively. The SIMO sonar adopts the up-sloping LFM pulse, i.e., with 390 kHz-410 kHz as the frequency band.

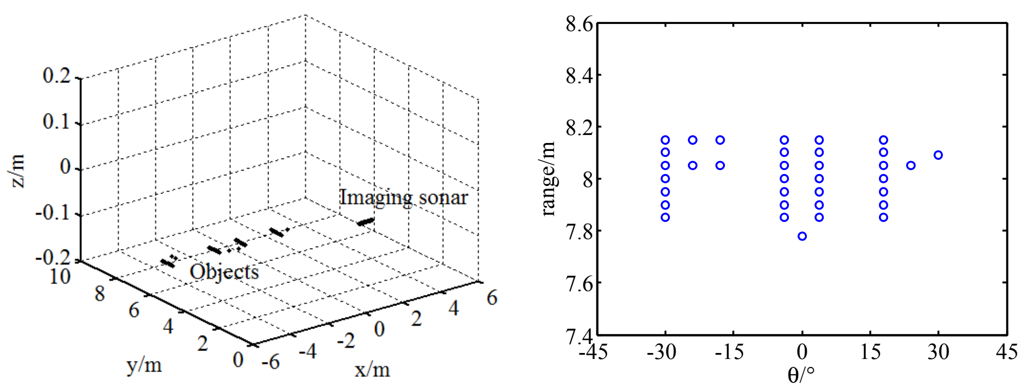

(a) (b)

Fig. 3. (a) Locations of objects and imaging sonar; (b) Objects.

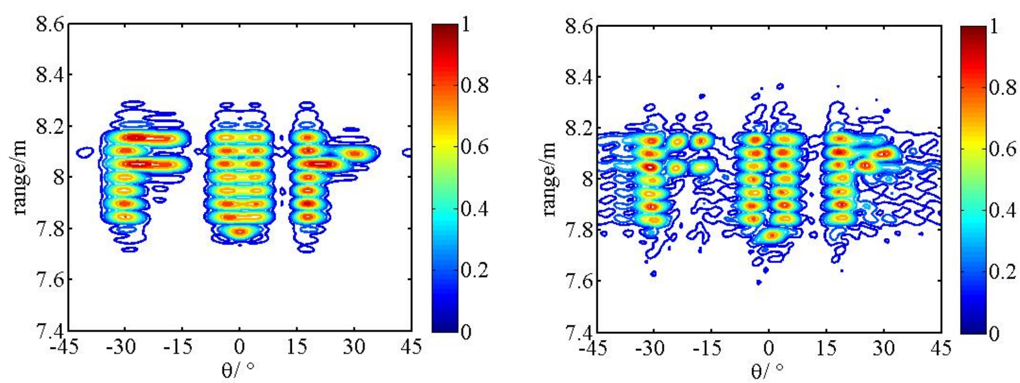

(a) (b)

Fig. 4. Imaging results of (a) SIMO sonar and (b) MIMO sonar

The objects, located on the plane of z=-0.2 m, are of equal unit strength and form three letters "Fur". The scattering coefficients of the background are set to 0.05. The locations of the imaging sonar and "Fur" are depicted in Fig. 3(a), and the planform of "Fur" is depicted in Fig. 3(b).

At the receiving end, echoes at all receiving sensors are obtained according to Eq. 10. And the signal-to-noise ratio (SNR) is set to 10 dB with a white Gaussian noise assumption. The sampling frequency is equal to 2000 kHz. The span of the beam steering direction is from -45° to 45° with 1° step. A Chebyshev window with -25 dB sidelobe level is applied to the phase-shifting beamformer. All the 2-D sector-scan imaging results have been normalized.

The 2-D imaging results of the SIMO and MIMO sonar are depicted in Fig. 4 (a) and (b), respectively. Since the two sonars use equal bandwidth transmitting pulses, the range resolutions are almost the same. However, the cross-range resolutions are not equal, even though the two sonars share the same physical size and sensor number. As depicted in Fig. 4(a), the scatterers of "Fur" cannot be separated along the x axis due to the poor cross-range resolution of the SIMO sonar. As depicted in Fig. 4 (b), all the scatterers of "Fur" are successfully imaged. From Fig.4, we can see that the MIMO sonar has better cross-range resolution than the SIMO sonar.

V. CONCLUSIONS

A 2-D sector-scan imaging approach based on a MIMO sonar composed of two transmitting sensors and a receiving ULA is proposed in this paper. The spacing between the two transmitting sensors is equal to the product of the inter-sensor spacing and the sensor number of the receiving ULA. Furthermore, to avoid using complicated coded waveforms (see, e.g., [6-12]), two narrowband LFM pulses are adopted. The two LFM pulses share the same frequency band but opposite modulation slopes (i.e, one is up-chirp pulse and the other is down-chirp pulse). The opposite modulation slopes ensure the independence property between trans- mitting waveforms and meanwhile, the same frequency band makes the transmitting waveforms have the same auto-correlation function. Thus, the outputs of matched filters can be considered pulse-compressed echoes of a virtual SIMO sonar with a two-time bigger aperture than the physical size of the MIMO sonar. Therefore, the MIMO sonar doubles the cross-range resolution without adopting larger-size array or higher-frequency waveforms, when compared to a real SIMO sonar with the same physical size and sensor number.

However, the mainlobe envelopes of pulse-compressed echoes reflected back from a single scatterer cannot remain in the same range bin. And hence, the adoption of the phase-shifting beamforming will cause relatively poor range- and cross-range resolutions and high sidelobe levels. The time delay beamforming can align delayed mainlobe envelopes of pulse-compressed echoes (i.e., the range alignment) and obtain the best range and cross-range resolutions. Nevertheless, it dramatically increases the computation burden at the receiving end. For a MIMO imaging sonar suffering from high computational matched filtering, the typical time delay beamforming is not suitable for the real-time imaging application. Therefore, applying other beamforming methods such as the shifted sideband beamforming to the MIMO imaging sonar is our next work.

ACKNOWLEDGMENT

This work was supported in part by the National Nature Science Foundation of China under Grant 11104222 and the Doctorate Foundation of Northwestern Polytechnical University under Grant CX201101.

REFERENCES

[1] J. L. Sutton, "Underwater acoustic imaging," *Proceeding of the IEEE*, vol. 67, no. 4, pp. 554-566, Apr. 1979.

[2] A. Pascoal, P. Oliveira, C. Silverstre, and *et al.*, "Robotic ocean vehicles for marine science applications—the European ASIMOV project," *In Proc. OCEANS 2000 MTS/IEEE Conf. and Exhibit.*, RI, USA, vol. 1, pp. 409-415, Sep. 2000.

[3] E. Desa, R. Madhan, P. Maurya," Potential of autonomous underwater vehicles as new generation ocean data platforms," *Current Science*, vol. 90, no. 9, pp. 1202-1209, May 2006.

[4] R. Henthorn, D. W. Caress, H. Thomas, and *et al.*, "High-resolution multibeam and subbottom surveys of submarine canyons, deep-sea fan channels, and gas seeps using the MBARI mapping AUV," *in Proc. OCEANS 2006*, Boston, USA, pp. 1-6, Sep. 2006.

[5] M. Soumekh, "Array imaging with beam steered data," *IEEE Trans. Image Process.*, vol. 1, no.3, pp. 379-390, Jul. 1992.

[6] J. Li, .Stoica, and X. Y. Zheng, "Signal synthesis and receiver design for MIMO radar imaging," *IEEE. Trans. Signal Process.*, vol. 56, no. 8, pp. 3959-3968, Aug. 2008.

[7] H. He, P. Stoica, and J. Li, "Designing unimodular sequence sets with good correlation-including an application to MIMO radar," *IEEE Trans. Signal Process.*, vol. 57, no. 11, pp. 4391-4405, Nov. 2009.

[8] D. W. Wang, X. Y. Ma, and Y. Su, "Two-dimensional imaging via a narrowband MIMO radar system with two perpendicular linear arrays," *IEEE Trans. Image Process.*, vol. 19, no. 5, pp. 1269-1279, May 2010.

[9] D. W. Wang, X. Y. Ma, A. L. Chen, and Y. Su, "High-resolution imaging using a wideband MIMO radar system with two distributed arrays," *IEEE Trans. Image Process.*, vol. 19, no. 5, pp. 1280-1289, May 2010.

[10] C. Z. Ma, T. S. Yeo, C. S. Tan, et al., "Three-dimensional imaging of targets using colocated MIMO radar," *IEEE Trans. Geos. Remote Sens.*, vol. 49, no. 8, pp. 3009-3021, Aug. 2011.

[11] X. H. Liu, C. Sun, J. Zhuo, and *et al.*, "Devising MIMO arrays for underwater 3-D short-range imaging," *in Proc. OCEANS'12 MTS/IEEE*, Hampton Roads, USA, Oct. 2012.

[12] X. H. Liu, C. Sun, F. Yi, and *et al.*, "Underwater three-dimensional imaging using narrowband MIMO array," *Science China in Phys. Mechan. Astron.,* vol. 56, no.7, pp. 1346-1354. Jul. 2013.